# Inversion of surficial sediment thickness from under-ice acoustic transmission measurement

Nicholas P. Chotiros, Gaute Hope, Espen Storheim, Halvor Hobaek, Lee Freitag, and Hanne Sagen

## ARTICLES YOU MAY BE INTERESTED IN

A seminal paper linking ocean acoustics and physical oceanography
The Journal of the Acoustical Society of America **148**, R9 (2020); https://doi.org/10.1121/10.0002761

Model-based convolutional neural network approach to underwater source-range estimation
The Journal of the Acoustical Society of America **149**, 405 (2021); https://doi.org/10.1121/10.0003329

Feit's seminal article on radiation of sound by a vibrating plate
The Journal of the Acoustical Society of America **149**, R1 (2021); https://doi.org/10.1121/10.0002422

Quantifying the contribution of ship noise to the underwater sound field
The Journal of the Acoustical Society of America **148**, 3863 (2020); https://doi.org/10.1121/10.0002922
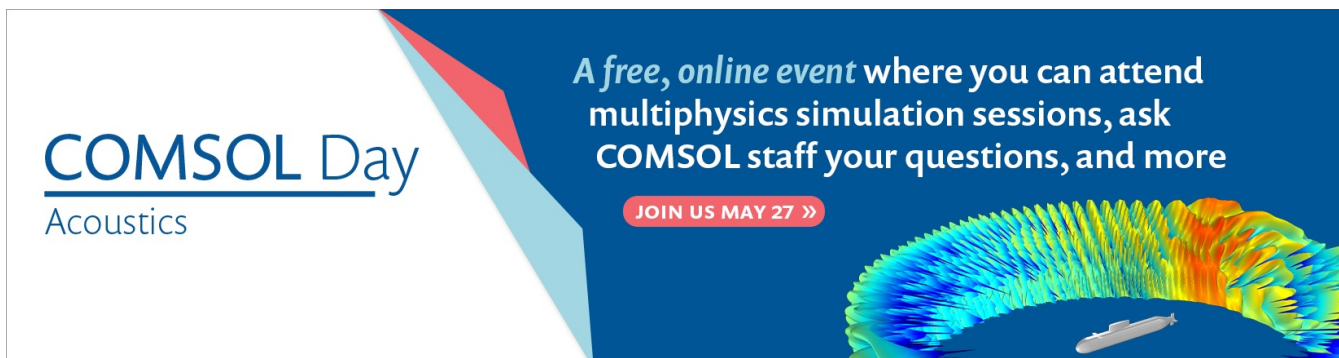
Temporal and spatial characteristics of the Beaufort Sea ambient noise environment
The Journal of the Acoustical Society of America **148**, 3928 (2020); https://doi.org/10.1121/10.0002955

Physics-based characterization of soft marine sediments using vector sensors
The Journal of the Acoustical Society of America **149**, 49 (2021); https://doi.org/10.1121/10.0002975

CrossMark
click for updates

# Inversion of surficial sediment thickness from under-ice acoustic transmission measurement[a)]

Nicholas P. Chotiros,[1,b)] Gaute Hope,[2] Espen Storheim,[3] Halvor Hobaek,[3] Lee Freitag,[4] and Hanne Sagen[3]

[1]*Applied Research Laboratories, University of Texas, Austin, Texas 78758, USA*

[2]*Norwegian Meteorological Institute, Oslo, Norway*

[3]*Nansen Environmental and Remote Sensing Center, Bergen, Norway*

[4]*Woods Hole Oceanographic Institution, Woods Hole, Massachusetts 02543, USA*

**ABSTRACT:**

The under-ice acoustic transmission experiment of 2013, conducted under ice cover in the Fram Strait, was analyzed for bottom interactions for the purpose of developing a model of the seabed. Using the acoustic signals, as well as data from other sources, including cores, gravimetric, refraction, and seismic surveys, it was deduced that the seabed may be modeled as a thin surficial layer overlaid on a deeper sediment. The modeling was based on the Biot–Stoll model for acoustic propagation in porous sediments, aided by more recent developments that improve parameter estimation and depth dependence due to consolidation. At every stage, elastic and fluid approximations were explored to simplify the model and improve computational efficiency. It was found the surficial layer could be approximated as a fluid, but the deeper sediment required an elastic model. The full Biot–Stoll model, while instrumental in guiding the model construction, was not needed for the final computation. The model could be made to agree with the measurements by adjusting the surficial layer thickness. © *2021 Acoustical Society of America.*
https://doi.org/10.1121/10.0003328

## I. INTRODUCTION

The Arctic seabed has not been extensively studied due to the difficulties and high cost of working in the Arctic environment. The Fram Strait seabed, which is the subject of this study, is often described as a sea ice sediment (SIS) because it is the result of sediments from high latitude continental shelves that were frozen in sea ice and deposited when the ice melted (Dethleff and Gesa, 2010). There is a distinction between the west and east Fram Strait due to the difference in their currents. On the west side of the strait, the east Greenland current flows southward carrying relatively cold water out of the Arctic. This side of the strait tends to have a greater sea ice coverage. It is speculated that western Fram Strait SIS clays came from East Siberian and North American shelf sources. The West Spitsbergen current brings warmer water up from the south along the east side of the strait, and the SIS on this side may have originated from the Kara Sea or the Laptev Sea, carried by ice that is entrained by the current. The UNDER-ICE experiment, as published by Hope *et al.* (2017), took place in September 2013, on the slope of the Fram Strait that is rising toward the east, but in the Greenland current since the ice is drifting south. It contains under-ice acoustic signals that interact with the seabed and therefore presents an opportunity for studying the seabed.

The organization of this study is as follows. In Sec. II, a description is given of the seabed based on published seismic surveys and core samples. In Sec. III, the UNDER-ICE experiment is revisited for the purpose of verifying the acoustic propagation model and extracting seabed-related acoustic signals. In Sec. IV, the seabed acoustic model is developed. A model based on the seismic survey data is shown to be too reflective to fit the measured data. The surficial layer is modeled both as a fluid and as a porous medium, and its reflection coefficient is shown to be too small to fit the measured values. Finally, a model that included a surficial layer over the deeper sediment was constructed that matches the measured signal. Concluding remarks are made in Sec. V.

## II. SEABED STRUCTURE

There have been a number surveys in the vicinity of the UNDER-ICE experiment conducted by the Alfred Wegener Institute for Polar and Marine Research. In Hope *et al.* (2017), the seabed model was based on a seismic survey by Jokat *et al.* (1995). In this reference, there were two survey tracks: one was about 200 km to the north of the acoustic paths, which included the western slopes of the Yermak Plateau (YP), and the other was about 200 km to the south. They found thin sedimentary cover with sound speeds starting at 1.7 km/s and reaching up to 4.6 km/s, for example, in

Fig. 3 of Jokat *et al.* (1995). To a seismologist, "thin" can mean several hundred meters. In this study, additional seismic survey data closer to the experiment area are used to construct a more detailed structure.

## A. Seismic survey measurements

The seabed under the Fram Strait may be divided into strata according to depth and age, according to Geissler *et al.* (2011). The UNDER-ICE experiment was conducted over an area that is considered to be an extension of the YP. The basement level, designated YP1, is more than 7 million years old (Ma). The next level, YP2 is between 2.6 and 7 Ma. The top layer, YP3, is less than 2.6 Ma, which is believed to be the start of the last ice age. The YP3 and YP2 layers are mostly the result of terrigenous sediments carried by ice sheets and deposited when the ice melted. YP3 is identified with the IA layer in the 910 and 911 cores of the Ocean Drilling Program (ODP). It is described as having a "transparent reflection character with some continuous reflectors" (Geissler and Jokat, 2004). YP2 is described as a "thick sequence of subparallel continuous reflectors" (Geissler *et al.*, 2011).

There are recent seismic survey lines that intersect the track of the UNDER-ICE receiver array, reported by Geissler *et al.* (2011), in particular, tracks 20040040 and 20040050, as shown in the top panel of Fig. 1. The receiver array is called the Integrated Ice Station (IIS). Their survey shows that, at a water depth of approximately 2 km, the combined YP3 and YP2 layer is about 1 km thick, as
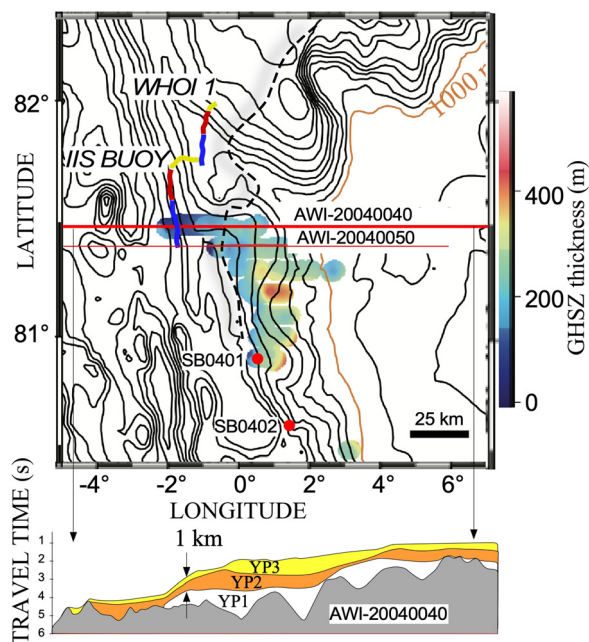


FIG. 1. (Color online) Top: UNDER-ICE source (WHOI1) and receiver (IIS) positions, published seismic survey tracks (AWI), and refraction measurement sites (SB). Ice cover to the left of the dashed curve. Isobath contour spacing 250 m. The seabed has potential to support gas hydrates: estimated GHSZ thickness color coded. Adapted from Geissler *et al.* (2014). Bottom: Sediment profile of track AWI-20040040 adapted from Geissler *et al.* (2011).

indicated in the bottom panel of Fig. 1. The refraction measurements conducted with the aid of sonobuoys, at nearby locations labeled SB0401 and SB0402 (Geissler *et al.*, 2011), indicate that the p-wave speed varies from 1.9 to 2.3 km/s from the top of YP3 to the bottom of the YP2 layer. The resolution is not good enough to see any detail in the profile; therefore, a linear p-wave speed profile is assumed. Below YP2, the p-wave speed jumps to 4 km/s.

Bulk density estimates are obtained from gravimetric inversion, specifically profile 99170 (Geissler and Jokat, 2004). Although this profile was in the Nansen Basin, rather than the Fram Strait, it is considered to be part of the YP and of the same sediment type. It indicates that bulk density varies from 2.1 to 2.4 g/cc from the top of YP3 to the bottom of YP2. A linear density profile is assumed. The most common solid mineral particles in sedimentary rocks are silicates with an average density, $\rho_r$, of approximately 2.7 g/cc, which is considerably higher. Therefore, the sediment must be treated as porous. The pore water density is approximately equal to that of the water just above the seabed. The measured density profile translates to a porosity that varies from 0.40 to 0.31. This is consistent with cores collected by Riedel *et al.* (2018) from the western slope of the Yermak Plateau (78° 33′ N, 9° 25′ E) that indicated an average porosity of 0.4 at depths below seafloor of up to 40 m. From the ODP, leg 151, which drilled a few cores to depths of 1 km below the seafloor in the Fram Strait, the sediment is mostly classed as silty clay, with little variation with depth. The sediment classification of "silty clay" effectively bounds the mean grain diameter between 1/16 and 1/256 mm according to the Wentworth scale (Wentworth, 1922). The geometric mean is 1/64 mm. Below YP2, the density jumps to 2.7 g/cc, which could be interpreted as solid sedimentary rock, but the p-wave speed is likely too low for that interpretation. A more likely composition is of a stiffer material, like an igneous or metamorphic rock with a density of 3 g/cc and a porosity of 0.15.

## B. Surficial layer

There are very few samples of seabed sediments in the Arctic because of the difficulties of working in the Arctic environment. An unlikely source of seabed information is a paper by Käss *et al.* (2019), describing a survey of macrofauna in the deep Fram Strait. They collected eight box cores from which water content and median grain diameter were measured. The values obtained are shown in Table I. The cores with labels "EG" are from the west side of the Fram Strait, while those marked "HG" are from the east. The latter appear to have a higher water content on average. Grain diameter values put the sediments in either the "very fine sand" or "silt" category, based on the Wentworth scale for grain size (Wentworth, 1922). The box cores were taken from coordinates approximately 200 km to the south of the acoustic paths and over a similar range of bottom depths, i.e., between 1000 and 2500 m. The average value of porosity is 0.56. It is consistent with another measurement by

TABLE I. Box core measurements from Käss *et al.* (2019) and computed parameters.

| Core | EG-I | EG-II | EG-III | EG-IV | HG-I | HG-II | HG-III | HG-IV |
|---|---|---|---|---|---|---|---|---|
| Water content | 0.54 | 0.46 | 0.43 | 0.43 | 0.66 | 0.62 | 0.52 | 0.51 |
| Median grain diameter ($\mu$m) | 13.4 | 15.1 | 20.3 | 88 | 17.4 | 17.8 | 22.9 | 26.3 |
| Depth (m) | 995 | 1548 | 1971 | 2603 | 1283 | 1540 | 1887 | 2462 |
| $M_z$ ($\phi$) | 6.22 | 6.05 | 5.62 | 3.51 | 5.84 | 5.81 | 5.45 | 5.25 |
| Porosity | 0.58 | 0.55 | 0.53 | 0.53 | 0.63 | 0.62 | 0.58 | 0.57 |
| Bulk density (kg/m$^3$) | 1726 | 1792 | 1820 | 1820 | 1647 | 1671 | 1742 | 1749 |
| Density ratio | 1.67 | 1.73 | 1.76 | 1.76 | 1.59 | 1.61 | 1.68 | 1.69 |

Stein (2005), from a location further south—core number PS66/341 (79° 44′ N, 0° 45′ W)—which showed values between 0.75 and 0.5 down to a depth below bottom surface of 3 m.

In Table I, the first three lines are from Käss *et al.* (2019). The remainder are computed parameters that are commonly used in sediment characterization. The grain size parameter $M_z$ is a popular parameter in the geophysics community. It is defined as the negative of log base 2 of the mean grain diameter in millimeters. It can have negative and positive values—larger positive values indicate smaller grain sizes. Most of the values are close to 6, which corresponds to a grain diameter of 1/64 mm, consistent with the previous estimate from the deep cores. The porosity is defined as the volume of pore fluid per unit volume of sediment. It is related to water content, which is the mass of water per unit mass of solid material. To calculate one from the other, the same values of densities of the water and the solid material are used as for the YP3 and YP2 layers. It is likely that the surficial layer and the YP3 and YP2 sediments are from the same source, hence the same grain size. They only differ in age and the degree of consolidation. The bulk density is simply the density of sediment, computed from the densities of the water and the solids in the proportions determined by the porosity. The density ratio is the bulk sediment density divided by the density of the water.

## III. MARGINAL ICE ZONE EXPERIMENT REVISITED

The UNDER-ICE experiment, as reported by Hope *et al.* (2017), is revisited to review the propagation model and to extract seabed interactions for the purpose of finding a plausible model of the seabed. In this experiment, an omnidirectional sound source, referred to as WHOI1, at a depth of 90 m under ice cover projected a linear frequency modulated signal centered at 900 Hz, with a bandwidth of 25 Hz. Its position is as shown in Fig. 1. The signal was received at a range of 32 km by a vertical array of four hydrophones, referred to as the IIS, at depths 15, 20, 25, and 30 m. The average ice thickness along the sound path was approximately 2 m, based on historical data. The OASES software for seismo-acoustic propagation in horizontally stratified waveguides (Schmidt, 2011) was used to construct a propagation model with which to compare the measured signals. The model used the measured sound speed profile and a nominal water depth of 2000 m. Based on historical

data, the ice is modeled as an elastic layer of average thickness 2 m, density 0.9 g/cc, p- and s-wave speeds 3600 and 1800 m/s, and attenuations 0.216 and 0.648 dB per wavelength, respectively. The sound speed profile in the water is as shown on the right of Fig. 2.

The model predicts a number of arrivals: a deep refracted arrival (D), the first bottom bounce arrival (A1), the twice bottom bounced arrival (A2), the three times bottom bounced ray (A3), and the surface duct arrival (B). The last was predicted to have the highest amplitude. The notional raypaths, overlaid on the modeled acoustic pressure field, along with the sound speed profile, are shown in Fig. 2. As in Hope *et al.* (2017), the signal from the deepest receiver, at a depth of 30 m, will be examined in detail.

A signal pulse was transmitted every hour during the experiment. The received signal was match-filtered and windowed with a Tukey ($a = 0.1$) filter. The Tukey parameter, $a$, indicates the tapered fraction of the frequency window. The intensity average of 15 pings and the standard deviation in dB are shown in Fig. 3. Three distinct arrivals are discernible in the data. In Hope *et al.* (2017), the first arrival was identified as A1 (the D arrival was thought to be almost coincident with A1 but weaker), and, since the model predicted the B arrival to be the strongest, the source level in the model was arbitrarily adjusted to match the measured level of the B arrival as shown in Fig. 12 of Hope *et al.* (2017). With hindsight, this was found to be inconsistent with the known source level of the sound projector, the D
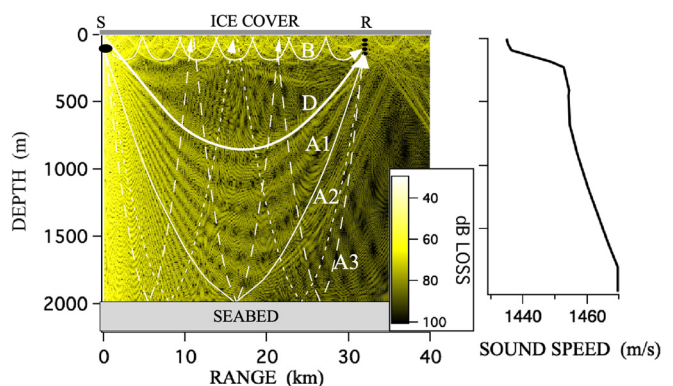


FIG. 2. (Color online) Raypaths A1, A2, A3, B, and D, superimposed on the acoustic pressure field computed using OASES (left) and the measured sound speed profile (right).
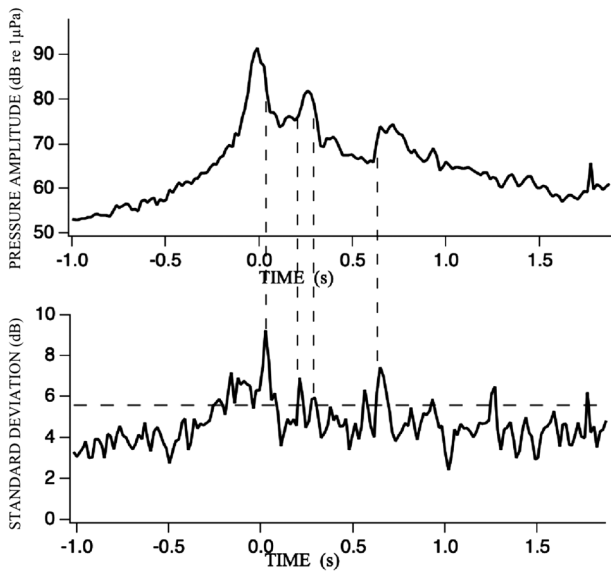
FIG. 3. Measured rms sound pressure amplitude (top), centered on the first arrival, and the standard deviation in dB (bottom). The dashed lines point to the increased standard deviation on the slopes of the signal peaks.

arrival was the first to arrive, and the B arrival was overestimated by the model.

## A. The deep refracted arrival (D)

In this section, the propagation model is validated against the known source level of the sound projector, the scattering by volume inhomogeneities is recognized, and problems with the under-ice sound channel are mitigated. On revisiting the model-data comparison, it became clear that the deep refracted arrival (D) was the dominant signal. Its prominence is consistent with previous observations that deep refracted rays are relatively stable and predictable (Worcester *et al.*, 1999). Its level and travel time are only dependent on the sound speed profile and unaffected by reflections at the surface and bottom. To study the D arrival in isolation, a model was constructed that consisted of the measured sound speed profile but without any boundaries, i.e., with neither surface nor bottom. The signal was given a source level (SL) of 183 dB re 1 $\mu$Pa, which is the known source level used in the experiment, and filtered with a Tukey window filter ($a = 0.1$), consistent with the processing of the experimental signal. The measured signal is compared with the Tukey window response, shown as curve (a) in Fig. 4. The measured pulse is very similar to the impulse response of the Tukey window, which indicates that the D arrival is essentially a single pulse.

It is noticed that the model pulse length in curve (a) is shorter than the measured pulse. Scattering by sound speed inhomogeneities and/or fluctuations in the water, due to turbulence, eddies, internal waves, and random temperature and salinity variations in the open ocean is known to increase pulse length. This subject has been extensively studied in the context of long-range underwater propagation. The approach used by Colosi *et al.* (1999) is very
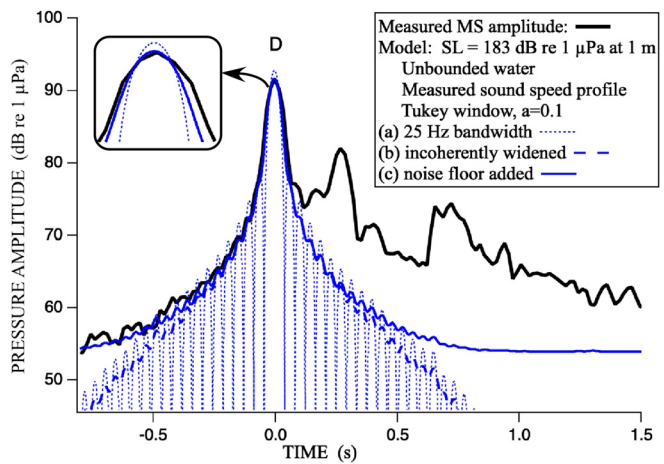


FIG. 4. (Color online) Comparison of measured pressure amplitude with models of the refracted arrival D in unbounded water, in which the signal spectrum is shaded by a Tukey window, with and without incoherent pulse widening due to scattering and a noise floor.

comprehensive but beyond the scope of this study. An adequate but simpler approach is taken, based on earlier work by Tarng *et al.* (1988). Their numerical investigations quantified the effect of scattering on random variations in the arrival time and the widening of the signal pulse, which increases with range. Random variations in arrival time also cause an increase in the standard deviation of the signal level on the slopes of the pulse peaks, as seen in the lower panel of Fig. 3. The pulse length increase is related to the mean-square refractive index variation $\langle \mu^2 \rangle$. The refractive index variations are assumed to have an isotropic Gaussian spatial correlation function with a characteristic correlation distance $l$. Tarng *et al.* (1988) identified a number of mechanisms including near-field scattering, out-of-plane scattering, and random phase perturbation. The most significant mechanism is the amplification of the scattering by the background sound speed gradient. This mechanism dominates at long ranges, and it is the only one considered here.

According to Eq. (42) of Tarng *et al.* (1988), the ratio of the mean-square pulse width increase, $w^2$, to the unperturbed width squared, $T_o^2$, is given as a function of range $x$ by Eq. (1),

$$\frac{\langle w^2 \rangle}{T_o^2} = \sqrt{\pi} \frac{16 \langle \mu^2 \rangle}{3l} \frac{bx^3}{c_o^2} \left( \frac{19}{160} bx^2 + \frac{11}{40} z_o \right). \qquad (1)$$

In this model, it is assumed that the sound path is entirely below the axis of the sound channel. In under-ice propagation, this is mostly true, since the axis of the sound channel is approximately at the ice-water interface. The term $z_o$ is the depth of the source relative to the axis. This term can be ignored because it is completely overwhelmed beyond a few kilometers by the other term. The term $c_o$ is the sound speed along the axis of the sound channel. The term $b$ is the normalized sound speed gradient, i.e., the sound speed gradient divided by $c_o$, and its value is

TABLE II. Parameters to determine pulse length increase.

| Parameter | Value |
|---|---|
| $\langle \mu^2 \rangle$, MS refractive index fluctuation | $1 \times 10^{-8}$ |
| $l$, correlation length (m) | 1.6 |
| $c_o$, sound speed in the channel axis (m/s) | 1469 |
| $b$, normalized sound speed gradient (m$^{-1}$) | $1 \times 10^{-5}$ |
| $z_o$, depth (m) | 90 |

approximately $10^{-5}$ m$^{-1}$ in this experiment. It plays a critical role in amplifying the effects of the random scattering. The mean-square refractive index fluctuations $\langle \mu^2 \rangle$ are depth dependent (Colosi *et al.*, 1999) with a peak value in the sound channel axis of around $10^{-6}$, but settling down to a lower level of about $10^{-7}$ and below at deeper depths. Medwin (1974) estimated that most of the quiescent fluctuation in the ocean is due to thermal inhomogeneities, and the effective value is around $10^{-8}$. Since most of the sound path associated with D is well below the channel axis, the lower value will be used in this model. The most difficult parameter is the correlation length $l$. This is because, in reality, the refractive index fluctuations take place at many scales, and it is impossible to properly represent it with a single scale parameter. However, acoustic signals tend to respond selectively to the scales that are closely matched to the acoustic wavelength. Therefore, the effective correlation length is as much a function of the acoustic frequency as it is of the environmental processes, and a value equal to the acoustic wavelength at 900 Hz is assumed. The values are shown in Table II. The plot of estimated pulse width as a function of range is shown in Fig. 5. It shows the root mean square (rms) pulse width increasing by a factor of approximately 3 at 32 km. Since the input parameters could be only approximately quantified, this should be regarded as an order of magnitude estimate. Comparing the width of curve (a) in Fig. 4 with the measured pulse, at the $-3$ dB points, it is determined that the measured pulse is about twice as wide as the model pulse. The increase in pulse length is an incoherent process, and it can be simulated by convolving the squared amplitude of the unperturbed Tukey filter response $|p_{t0.1}|^2$ with a Gaussian function of the appropriate width $\tau$. The widened pulse $p_w(t)$ is given in terms of intensity by
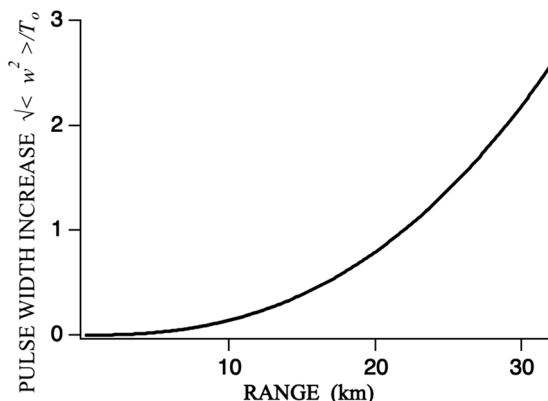
$$\frac{|p_w(t)|^2}{2\rho c} = \frac{|p_{t0.1}(t)|^2}{2\rho c} \otimes \frac{e^{-1/2(t/\tau)^2}}{\tau\sqrt{2\pi}}. \qquad (2)$$

This equation conserves energy, which means that the widened pulse will have a peak amplitude that is lower than the unperturbed pulse. The widened pulse is shown in curve (b) in Fig. 4. The value of $\tau$ is 0.03 s. The pulse widening process also has the effect of smoothing out the ripples in the sidelobes of the Tukey filter response. The result is a very good fit to the measured pulse in the vicinity of the peak and down to about 20 dB below the peak. If an incoherent background noise floor of 53 dB is added, the result is a very good fit at all points preceding the peak, as shown in curve (c). Given the correlation processing gain of 23 dB and the bandwidth of 25 Hz, this noise floor corresponds to an ambient noise spectrum level of 59 dB re 1 $\mu$Pa rms per Hz—equivalent to sea state 3.

## B. The main surface channel arrival (B)

The D and B arrivals may be modeled by using the sound speed profile in water, with ice cover, but without a bottom. This is shown in curve (a) of Fig. 6. It is clear that the B arrival is greatly over-estimated by the model, and its sidelobes extend beyond its immediate vicinity, making it difficult to use the model to simulate the bottom returns. It is not the purpose of this study to address the B arrival in any depth, but, within the context of the OASES model, it can be brought into a semblance of agreement by allowing a certain level of additional attenuation (0.0055 dB per wavelength) in the top water layer (from the ice down to a depth of approximately 50 m) above and beyond the usual attenuation in seawater, as shown in curve (b) of Fig. 6.

Although curve (b) is approximately of the same level as the measured signal, the shape of the peak at B is significantly different, and the sidelobes before the peak of the D



FIG. 5. Increase in pulse width according to Tarng *et al.* (1988).
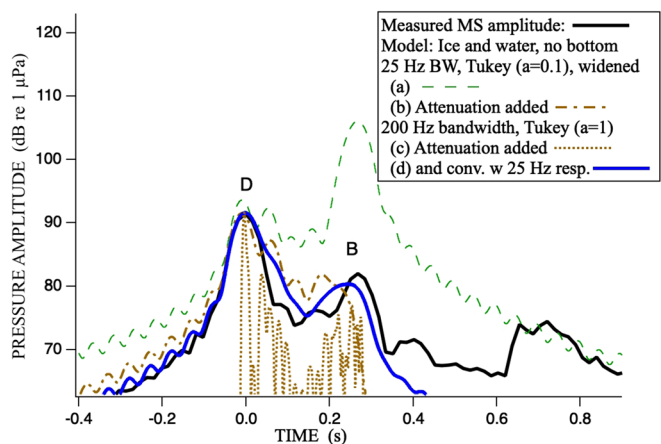


FIG. 6. (Color online) Water with sound speed profile and ice cover (no bottom). (a) Model of the 25 Hz bandwidth, Tukey ($a = 0.1$) filtered signal; (b) same as (a) but with attenuation in the top water layer; (c) same as (b) but at 200 Hz bandwidth, Tukey ($a = 1$) filter, showing numerous arrivals in the vicinity of B; (d) the intensity signal in (c) convolved with the impulse response of a 25 Hz, Tukey ($a = 0.1$) pulse, to simulate the incoherent summation of multiple arrivals and added background noise.

arrival continue to be higher than the measured values. An exploratory high-bandwidth simulation, which uses a 200 Hz bandwidth signal and a Hamming filter to reduce the sidelobes and isolate the individual arrivals, shows that, while the D arrival appears to be a single pulse, the B arrival is composed of several arrivals close together in time, as shown in curve (c). This also applies to the structure between D and B. In the 25 Hz bandwidth simulation, curve (b), the arrivals are added coherently according to the simulated propagation model, without any random scattering that exists in the real environment. This subject was touched upon earlier when the increase in pulse width of the D arrival was addressed. In addition to the pulse length increase, the scattering also causes decorrelation of the individual arrivals, such that the phase relationships between them are degraded. Therefore, they would not add in a coherent and predictable way as in the simulation model. To approximate the loss of coherence, the intensity of the 200 Hz bandwidth simulation is used to represent the arrival structure and convolved with curve (b) in Fig. 4, which represents the impulse response of a single pulse at the 25 Hz bandwidth, to obtain a more realistic representation of the B arrival, as shown in curve (d). The shape of this curve, in the vicinity of B, is closer to the measured signal envelope, and the sidelobe level before the peak of the D arrival is in agreement with the measured values as well.

The cause of the additional attenuation and its specific details are beyond the scope of this paper. If one may speculate, it probably represents the effect of ice keels that tend to obstruct the sound paths that are close to the ice but leave the steeper refracted and bottom bounced paths relatively undisturbed. Ice keels and similar features are beyond the capability of OASES 3.1. The above procedure provides an approximate fit so that the main purpose of this paper, i.e., the bottom model, may be developed. The B arrival may be analyzed in detail in a later study. The convolution of the high-bandwidth intensity model with the intensity impulse response of a single pulse at the 25 Hz bandwidth is a useful method for emulating the effects of random scattering, and it will be used for the bottom reflected signals in Sec. IV.

## IV. FINDING A BOTTOM MODEL TO FIT THE MEASUREMENT

In this section, bottom models are developed and compared to the measured bottom reflected signals. It is found that the bottom has to be modeled as surficial layer over a deeper sediment. Since the seismic survey and various core samples showed that the bottom is a porous medium, it would be appropriate to start with a porous medium model and find elastic or fluid approximations where possible.

### A. Porous medium sediment model

From the above description of the sediment, particularly the grain size, the rather low porosity, and high p-wave speed, which suggest that it is consolidated, it is appropriate that the sediment model should be based on Biot's theory,

and it would be more useful to express the density changes in terms of porosity changes. The porosity $\beta$ is defined as the volume of pore fluid per unit volume of sediment. It is related to bulk density $\rho$ through the densities of the solid and fluid components.

$$\rho = \beta\rho_f + (1 - \beta)\rho_r. \tag{3}$$

The most common solid mineral particles in sedimentary rocks are silicates with an average density, $\rho_r$, of approximately 2.7 g/cc. The water density, $\rho_f$, is determined by temperature, salinity, and depth, and it is estimated to be 1.035 g/cc at the bottom of the Fram Strait. These values suffice for the YP3 and YP2 layers, but not for YP1, because its density is significantly higher than that of the silicates. It may be composed of a denser material, possibly igneous or metamorphic—a density of 3 g/cc and a porosity of 0.15 is a combination that would fit the bulk density, as suggested earlier. In the absence of any further details, a linear increase in p-wave speed and density (expressed in terms of porosity) with depth is assumed in the YP3 and YP2 layers, as indicated in Fig. 7. There are no published measurements of the s-wave speed. It will be addressed with the aid of models.

The Biot model simulates wave propagation in a porous medium. There is no need to delve into the Biot equations, because they have already been integrated into the OASES software. To be precise, the Biot–Stoll version (Stoll and Kan, 1981) was incorporated into OASES, as described in Sec. 4.1.3 "Porous Media" on page 20 of the manual for OASES v3.1 (Schmidt, 2011). The user has to provide the input parameters of the Biot–Stoll model, and the software will take care of the reflection and transmission computations. Therefore, the main effort here is to estimate the input parameters of the Biot–Stoll model, which are listed in the top 13 lines of Table III. For completeness, the input parameters of the corresponding elastic and fluid models are also listed in the same table. This is a daunting list, but the development of the Biot theory has come a long way since the Biot–Stoll model, and there are new methods to estimate the parameters from grain size and porosity. The latest version is called the corrected Revil extended Biot (CREB) model (Chotiros, 2017). The Revil relationships allow the fluid dynamic parameters to be estimated from geophysical parameters, particularly porosity and mean grain size, and additional parameters that are well constrained, i.e., the cementation exponent and the shape parameter; the latter quantifies the effect of the shape of the pores. It is well developed for mono-size granular media, particularly the various grades of sands. It can cope with a moderate distribution of grain sizes. For the finer grains, such as silt and clay, it is still a work in progress. The CREB model is able to account for the frequency dependence of the Biot–Stoll parameters and, therefore, may be used for narrow- and wide-band signals. It is backward compatible with the Biot–Stoll model, and it can be used to generate the Biot–Stoll parameters. For narrow-band applications, the

376    J. Acoust. Soc. Am. **149** (1), January 2021
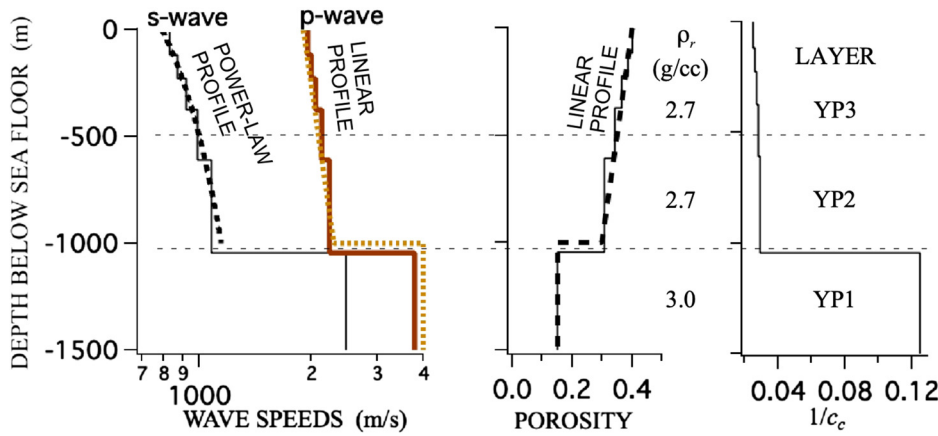
Chotiros *et al.*

FIG. 7. (Color online) Sediment model showing measurements of p-wave speed (left) and porosity profiles (middle) and inverted profiles of s-wave speed (far left), and consolidation (far right), including the stepwise approximation used in the numerical implementation.

Biot–Stoll model with constant parameter values is expected to be adequate.

For the purpose of modeling the shear wave speed profile in the sediment, a connection between the low-frequency bulk and shear moduli of a granular medium through the Hertz–Mindlin grain contact theory is used. The contact stiffness may be up-scaled to the macroscopic bulk and shear moduli, using the relationships developed by Walton (1987) and reformulated in the Rock Physics Handbook (Mavko *et al.*, 1998) and also found in Bachrach *et al.* (2000). The low-frequency asymptotic shear $G_o$ and bulk $K_{bo}$ moduli are real and simply related by Poisson's ratio of the solid material $\nu_r$, which is around 0.3, by

$$G_o = K_{bo} \frac{3(5 - 4\nu_r)}{5(2 - \nu_r)}. \tag{4}$$

The shear speed profile as a function of depth is predicted by the Hertz–Mindlin grain contact theory to follow a power-law relationship. Hamilton (1980) showed examples of measured shear speeds $c_s$ for silts and sands as a function of depth $d$ that may be fitted to a power-law relationship of the form,

$$c_s = c_{s0}(d_0 + d)^{\alpha}. \tag{5}$$

The shear speed at the top of the sediment $c_{s0}d_0^{\alpha}$ and the depth offset $d_0$ are constants to be determined. A non-zero depth offset $d_0$ indicates over-consolidation. The exponent $\alpha$, in theory, should be 1/6, but in practice, it varies between 1/4 and 1/3. In Hamilton's measurements it is closer to 1/3.

Finally, the consolidation theory of Pride (2005) relates the depth dependence of the sediment properties to porosity. Pride introduced a consolidation parameter $c_c$, which quantifies the consolidation—the degree of compaction of a granular sediment. It relates the low-frequency bulk modulus of the skeletal frame $K_{bo}$ to the bulk modulus of the solid material $k_r$ and porosity $\beta$,

$$K_{bo} = k_r \frac{1 - \beta}{1 + c_c \beta}. \tag{6}$$

The value of $c_c$ is the inverse of consolidation. It may range from 0, which indicates perfect consolidation, also known as the Voigt bound, to infinity, which indicates zero consolidation, i.e., no mechanical contact between the grains at all. The values of the bulk modulus of the solid grains $k_r$ and the pore water $k_f$ are 32 and 2.24 GPa, respectively.

For practical frequencies, the frame bulk $K_b$ and shear $G$ moduli are complex and frequency dependent. The associated loss mechanism is the quirt flow of pore fluid at the grain-grain contact. The real and imaginary parts of $K_b$ and $G$ are computed at the center of the frequency band, in this case 900 Hz. In the OASES implementation of the Biot–Stoll model, the imaginary parts of $K_b$ and $G$ are input as frame attenuations, $a_s$ and $a_c$, with the dimensions of dB per wavelength, and computed as the ratio of the imaginary part to the real part multiplied by $20\pi\log(e)$.

The remaining parameters of the Biot–Stoll model are estimated from the porosity and the average grain size. The sediment classification of "silty clay" from the deep cores of the ODP effectively bounds the mean grain diameter between 1/16 and 1/256 mm according to the Wentworth

TABLE III. Input parameters: Top, the Biot-Stoll model (GBS), and bottom, the elastic (GBSE) and fluid (GBSF) approximations.

| Description | Symbol | Value |
|---|---|---|
| Density of the pore fluid | $\rho_f$ (g/cc) | 1.037 |
| Bulk modulus of the pore fluid | $k_f$ (Pa) | $2.24 \times 10^9$ |
| Fluid viscosity | $\eta$ (Pa-s) | 0.0018 |
| Density of the solid constituent | $\rho_r$ (g/cc) | 2.7 |
| Bulk modulus of the solid constituent | $k_r$ (Pa) | $3.2 \times 10^{10}$ |
| Porosity | $\beta$ | 0.4 |
| Frame permeability | $\kappa$ (m²) | $1.65 \times 10^{-15}$ |
| Pore size | $a_p$ (m) | $4.76 \times 10^{-7}$ |
| Frame shear modulus | $\mathrm{Re}(G)$ (Pa) | $1.40 \times 10^9$ |
| Frame bulk modulus | $\mathrm{Re}(K_b)$ (Pa) | $1.16 \times 10^9$ |
| Frame s-wave attenuation | $\alpha_s$ (dB/$\lambda$) | 0.64 |
| Frame p-wave attenuation | $\alpha_p$ (dB/$\lambda$) | 1.6 |
| Tortuosity | $c_m$ | 6.87 |
| P-wave speed | $c_p$ (m/s) | 1953 |
| S-wave speed | $c_s$ (m/s) | 830 |
| P-wave attenuation | $\alpha_p$ (dB/$\lambda$) | 0.327 |
| S-wave attenuation | $\alpha_s$ (dB/$\lambda$) | 0.645 |
| Bulk density | $\rho$ (g/cc) | 2.035 |

J. Acoust. Soc. Am. **149** (1), January 2021

Chotiros *et al.* 377

scale (Wentworth, 1922). The geometric mean will be used, which is 1/64 mm. To avoid interrupting the narrative, the remaining parameters in the Biot–Stoll model are addressed in Appendix A.

Given the porosity profile in the middle panel of Fig. 7 and the p-wave speed in the left panel, the consolidation parameter $c_c$ may be inverted from the p-wave speed through the Biot–Stoll model and Eq. (6). The inverse of $c_c$ is plotted in right panel of Fig. 7, showing a linear increase in consolidation with depth in YP3 and YP2, and a step increase from YP2 to YP1.

Using Eq. (4), the frame shear modulus was estimated, and the shear speed was computed as a function of depth, as shown in the left panel alongside the p-wave speed profile in Fig. 7. Without any adjustment, it appears to fit a power-law function of the form shown in Eq. (5), consistent with the measurements of Hamilton (1980), where $\alpha = 1/3$, $c_{s0}d_0^\alpha = 794$ m/s, and $d_0 = 500$ m. The last value suggests a high degree of over-consolidation.

A stepwise approximation is used to model the continuous trends for the purpose of numerical modeling. Three versions of the Geissler data driven Biot–Stoll seabed model were formulated: the full Biot–Stoll model (GBS), an elastic approximation (GBSE), and a fluid approximation (GBSF). The last two approximations use the same bulk density, wave speeds, and attenuations as the Biot–Stoll model. The fluid approximation has zero shear wave speed.

The plain wave reflection function (OASR) of the OASES software suite was used to compute the reflection coefficients of the layered Biot–Stoll model as a function of grazing angle at the frequency of interest, i.e., 900 Hz. At this frequency, it was found that only the top layer was significant. Therefore, only the parameters of the top layer are listed in Table III. Nevertheless, it is useful to go through the design process for all the layers for completeness and to be sure that nothing significant has been missed. The reflection magnitude as a function of the grazing angle of the Biot–Stoll model and the corresponding elastic and fluid approximations are shown in Fig. 8. It is evident that the Biot–Stoll model and elastic approximation are indistinguishable, but the fluid approximation is very different, indicating that the shear wave plays an important part and should not be neglected.

## B. Bottom reflected signal structure

Using the sediment model, a simulation of the first bottom bounce on its own may be obtained by computing the high-bandwidth baseline model of water and bottom, but without any ice or surface. The water depth was adjusted to 2.26 km to make the model A2 arrival coincide with the measured A2 peak. The result, in curve (a) of Fig. 9, shows the single D and A1 arrivals cleanly separated. A high-bandwidth model that included the bottom was coherently subtracted from the same model but without a bottom, to isolate the bottom-related signals, as shown in curve (b). Comparing curves (b) and (a), it is evident that without the ice or surface, there is only one bottom arrival at A1, but in
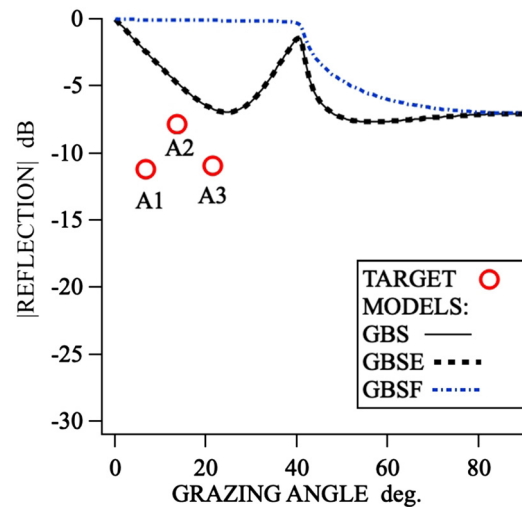


FIG. 8. (Color online) The target reflection coefficients and the computed reflection curves from the Biot–Stoll model (GBS) and its elastic (GBSE) and fluid (GBSF) approximations.

the presence of ice or surface, there are three additional arrivals, as shown in the inset. These arrivals are likely to be decorrelated by random scattering; therefore, they should be incoherently summed. As before, this is achieved by convolving the high-bandwidth intensity with the intensity of the impulse response at the 25 Hz bandwidth, and the result is shown in curve (c). Finally, the total high-bandwidth signal is convolved with the 25 Hz bandwidth response to obtain the ensemble average, shown in (d), for comparison with the measured signal. It is evident that the bottom model constructed from the seismic data produces a signal that is too large compared to the measured signal.

From the mismatch between the measured and modeled bottom-related signals, A1, A2, and A3 in Fig. 9, the target bottom reflection coefficients at the corresponding angles were estimated, as shown in Fig. 8. The overestimation of bottom reflection suggests that there must be a thin surficial



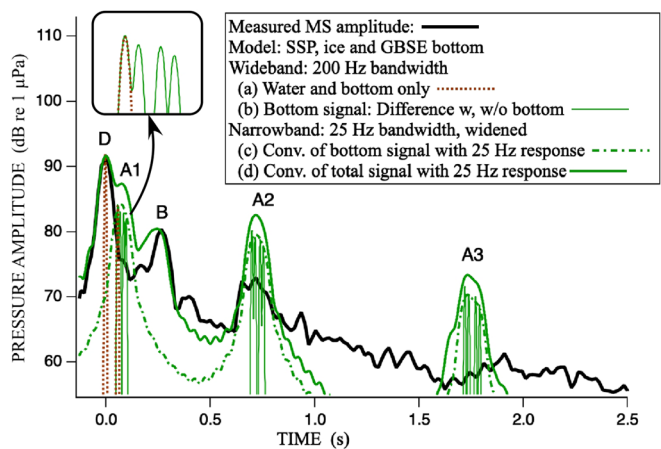FIG. 9. (Color online) Simulation of the GBSE bottom response: (a) high-bandwidth signal, without ice or surface; (b) bottom only signal from coherent subtraction of high-bandwidth models with and without bottom; (c) convolution of intensity in (b) with the 25 Hz bandwidth response; and (d) convolution of total high-bandwidth signal with the 25 Hz bandwidth response.

378    J. Acoust. Soc. Am. 149 (1), January 2021

Chotiros et al.

TABLE IV. Fluid model based on grain size relationships on pp. 313–314 of Jackson and Richardson (2006).

| Core | EG-I | EG-II | EG-III | EG-IV | HG-I | HG-II | HG-III | HG-IV | KJR |
|---|---|---|---|---|---|---|---|---|---|
| Density ratio | 1.15 | 1.15 | 1.15 | 1.27 | 1.15 | 1.15 | 1.15 | 1.15 | 1.673 |
| Sound speed ratio | 0.99 | 0.99 | 1 | 1.06 | 0.99 | 0.99 | 1 | 0.99 | 1.0 |
| Attenuation (dB/m/kHz) | 0.13 | 0.14 | 0.21 | 0.63 | 0.16 | 0.17 | 0.26 | 0.34 | 0.367 |

layer of softer sediment that is unaccounted for. Seismic surveys typically use frequencies below 100 Hz. Since the underwater acoustic wavelength at this frequency is 15 m, it is doubtful that a seismic survey would be able to detect a surficial sediment layer that is a few meters thick. Other possible causes for the reduction in signal level include increased shear speed and rough interface scattering, but they are unlikely due to the enhanced reflection at A2. The increased shear speed hypothesis is not feasible because the enhanced reflection that it brings is in the vicinity of the critical angle, and the angle at A2 is far from the critical angle. The rough surface hypothesis requires a periodic interface ripple that produces Bragg scattering at the A2 angle. This may randomly happen at one location, but it is rather unlikely when averaged over several pings while the projector and receiver are drifting over different parts of the bottom. Therefore, the surficial layer is the most likely solution.

### C. Fluid surficial layer approximation

Hamilton (1980) was one of the pioneers of seafloor modeling. He started with the approximation that the surficial seafloor sediment may be modeled as a fluid, defined by its density and sound speed. His measurements indicated that the sound speed was correlated with grain size and that attenuation, in dB/m, increased linearly with frequency. The APL-UW High-Frequency Ocean Environmental Acoustic Models Handbook (Applied Physics Laboratory, University of Washington, 1994) followed in the same direction, with a table linking grain size to density, sound speed, and attenuation [Table 2, Chapter IV of Applied Physics Laboratory, University of Washington (1994)]. Sound speed was

assumed to be independent of frequency. This is simple and very powerful because it means that the reflection coefficient is independent of frequency and a single set of parameters may be used over a wide range of frequencies. However, it is non-causal because attenuation must be accompanied by a change in sound speed. Buckingham (2007) improved upon this model with the grain-shearing and viscous grain-shearing models, which contained small changes in sound speed that satisfy causality. These models are described in the reference book by Jackson and Richardson (2006). For the computation of bottom reflection coefficient, Jackson and Richardson (2006) (pp. 213–214) provide a set of relations that permit density, sound speed, and attenuation to be estimated from the mean grain size, $M_z$, to be used with the Rayleigh reflection equation in a fluid approximation of the seabed. These relationships are reproduced in Appendix B.

Using these relationships and the $M_z$ values from the measurements in Table I, the seabed density, sound speed ratio, and attenuation were estimated, as shown in Table IV. It is noticed that the density ratio in Table I, which was computed from measured water content, is different from the density ratio in Table IV, predicted by the $M_z$ relationships. Even though the sediment density ratio in Table I is based on measurement and more accurate, the density ratio provided by the $M_z$ relationship is preferred. The reason is because the Rayleigh reflection equation is inaccurate when applied to the seabed, and the $M_z$ relationship provides a value for density ratio that is designed to compensate for the shortcomings of the Rayleigh reflection equation. These values were used to compute the half-space reflection loss curves, as shown in the left panel of Fig. 10.
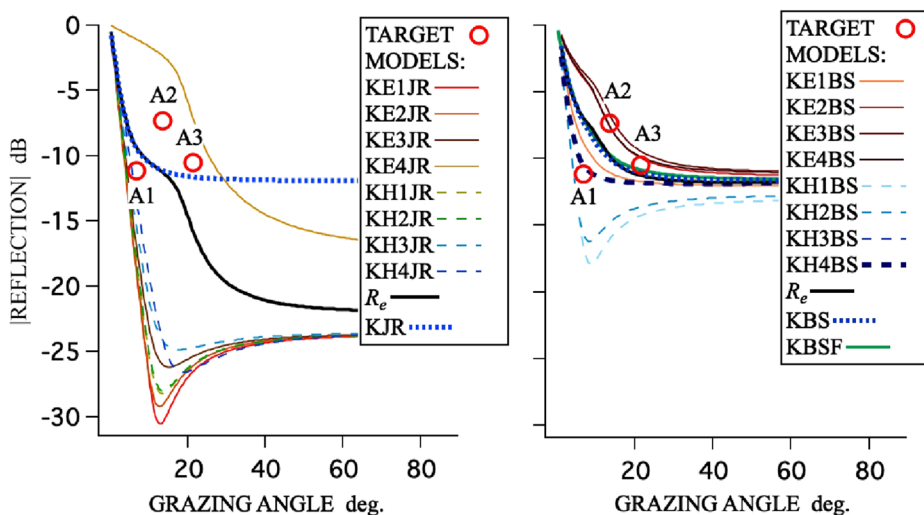


FIG. 10. (Color online) Plane-wave reflection amplitude as a function of grazing angle of the Jackson–Richardson fluid models (left) and Biot–Stoll models (right) based on grain size and porosity data in Table I.

The curves are labeled KEnJR and KHnJR, where n is a number from 1 to 4, corresponding to the EG and HG cores, respectively. Most of the reflection curves are well grouped except for the one from the EG-IV core, labeled as KE4JR. This appears to be because the grain size from this core is significantly larger compared to the others. The value of the expected reflection loss $R_e$ was computed as the intensity average of the eight curves. The resulting curve is clearly skewed by the one outlier, and the expected reflection coefficient is not easily replicated with a simple fluid half-space model. However, noting that the grazing angles that matter are between 0° and 20°, a half-space model was fitted to this range of values by hand, labeled as KJR. Its parameter values are as shown in the last column of Table IV, and it matches $R_e$ within these angles. Most of the curves are close to the target reflection coefficient at A1, and KJR is close to A1 and A3, but none of them can match all three target reflection coefficients. Therefore, a simple fluid half-space bottom is not going to be sufficient.

### D. Porous medium model of surficial layer

The Biot–Stoll parameters were estimated from the mean grain size and the porosity of the surficial layer. The details of the method are given in Appendix A. The resulting Biot–Stoll parameter values, in the units required for OASES, are shown in Table V.

The reflection curves for the six box cores are shown in the right panel of Fig. 10. The curves are labeled KEnBS and KHnBS, where n is a number from 1 to 4, corresponding to the EG and HG cores, respectively. It is observed that the curves are well grouped. The curves for the HG cores exhibit an intromission angle, while the EG cores show a critical angle. As before, the value of the expected reflection loss $R_e$ was computed using the average of the six curves, and the best-fit Biot Stoll model was found by hand. Due to the tight grouping of the eight curves, it was relatively simple to find a Biot–Stoll parameter set that matched the average reflection curve in its entirety, and it is labeled KBS, shown as the last column in Table V. It is also clear that none of the curves can match the target reflection values.

The next step is to consider a surficial layer over the sediment.

### E. Surficial layer over porous sediment

It is evident from Fig. 10 that a half-space of any of the surficial models will not provide the desired reflection coefficients for A1, A2, and A3, and a surficial layer over the sediment model needs to be considered. For the surficial layer, it is a choice between the Jackson–Richardson fluid model or the Biot–Stoll model. The rather artificial value of density used in the Jackson–Richardson model to achieve the required half-space reflection coefficient makes it unsuitable for use in a layered structure, because the desired reflection loss is obtained at the expense of a distorted transmission coefficient. Therefore, the Biot–Stoll model will be used. The first candidate is the average surficial Biot–Stoll model, KBS, over the sediment model GBS. However, since both of them have a higher reflection coefficient than the target value for A1, it is unlikely that the combination will suffice. Looking at the reflection curves in the right-hand side of Fig. 10, the model KH4BS based on the HG-IV core passes through the target value at A1. On the assumption that at shallow grazing angles, the surficial layer is dominant, this model would be a good candidate for the surficial layer. The choice of KH4BS is consistent with the location of the experiment being on the east slope of the Fram Strait.

A 4.8 m layer of the KH4BS surficial layer over the GBS sediment was found to fit the target coefficients at all three angles, A1, A2, and A3, as shown in Fig. 11. This is consistent with measurements by Stein (2005) from a location further south—core number PS66/341 (79° 44′ N, 0° 45′ W)—which showed porosity values close to the surficial layer down to a depth below bottom surface of 3 m. The resulting signal levels are compared to the measured levels in Fig. 12. The measured A1 signal is overshadowed by D, and it is only possible to identify its upper limit, and the model fits within the upper limit. The model A2 signal level is in good agreement with the measurement, but the measured width is a little wider than the model, most likely because of bottom depth variations in the experiment. The

TABLE V. Biot–Stoll parameters estimated from box cores from Käss et al. (2019).

| Core | EG-I | EG-II | EG-III | EG-IV | HG-I | HG-II | HG-III | HG-IV | KBS |
|---|---|---|---|---|---|---|---|---|---|
| $\rho_f$ (g/cc) | 1.037 | 1.037 | 1.037 | 1.037 | 1.037 | 1.037 | 1.037 | 1.037 | 1.037 |
| $k_f$ (Pa) | $2.24 \times 10^9$ | $2.24 \times 10^9$ | $2.24 \times 10^9$ | $2.24 \times 10^9$ | $2.24 \times 10^9$ | $2.24 \times 10^9$ | $2.24 \times 10^9$ | $2.24 \times 10^9$ | $2.24 \times 10^9$ |
| $\eta$ (Pa-s) | 0.001 | 0.001 | 0.001 | 0.001 | 0.001 | 0.001 | 0.001 | 0.001 | 0.001 |
| $\rho_s$ (g/cc) | 2.70 | 2.70 | 2.70 | 2.70 | 2.70 | 2.70 | 2.70 | 2.70 | 2.70 |
| $k_r$ (Pa) | $3.20 \times 10^{10}$ | $3.20 \times 10^{10}$ | $3.20 \times 10^{10}$ | $3.20 \times 10^{10}$ | $3.20 \times 10^{10}$ | $3.20 \times 10^{10}$ | $3.20 \times 10^{10}$ | $3.20 \times 10^{10}$ | $3.20 \times 10^{10}$ |
| $\beta$ | 0.58 | 0.54 | 0.53 | 0.53 | 0.63 | 0.62 | 0.58 | 0.57 | 0.56 |
| $\kappa$ (m$^2$) | $2.07 \times 10^{-14}$ | $1.58 \times 10^{-14}$ | $3.46 \times 10^{-14}$ | $8.77 \times 10^{-12}$ | $1.07 \times 10^{-13}$ | $9.18 \times 10^{-14}$ | $1.13 \times 10^{-13}$ | $1.71 \times 10^{-13}$ | $1.65 \times 10^{-12}$ |
| $a$ (m) | $9.85 \times 10^{-7}$ | $9.44 \times 10^{-7}$ | $1.38 \times 10^{-6}$ | $1.62 \times 10^{-5}$ | $1.89 \times 10^{-6}$ | $1.81 \times 10^{-6}$ | $2.15 \times 10^{-6}$ | $2.61 \times 10^{-6}$ | $4.22 \times 10^{-6}$ |
| $Re(G)$ (Pa) | $1.07 \times 10^7$ | $1.87 \times 10^7$ | $1.89 \times 10^7$ | $1.81 \times 10^7$ | $4.76 \times 10^6$ | $5.84 \times 10^6$ | $9.64 \times 10^6$ | $9.55 \times 10^6$ | $1.38 \times 10^7$ |
| $Re(Kb)$ (Pa) | $1.23 \times 10^8$ | $1.14 \times 10^8$ | $8.65 \times 10^7$ | $4.63 \times 10^7$ | $1.01 \times 10^8$ | $9.90 \times 10^7$ | $7.53 \times 10^7$ | $6.27 \times 10^7$ | $8.67 \times 10^7$ |
| $a_s$ (dB/$\lambda$) | 15.62 | 18.63 | 24.69 | 20.60 | 13.75 | 15.77 | 22.69 | 24.03 | 19.97 |
| $a_c$ (dB/$\lambda$) | 18.07 | 20.49 | 28.41 | 42.46 | 24.01 | 24.57 | 32.29 | 37.36 | 29.00 |
| $c_m$ | 3.42 | 3.83 | 3.64 | 1.97 | 2.65 | 2.76 | 2.94 | 2.84 | 3.04 |

380    J. Acoust. Soc. Am. **149** (1), January 2021
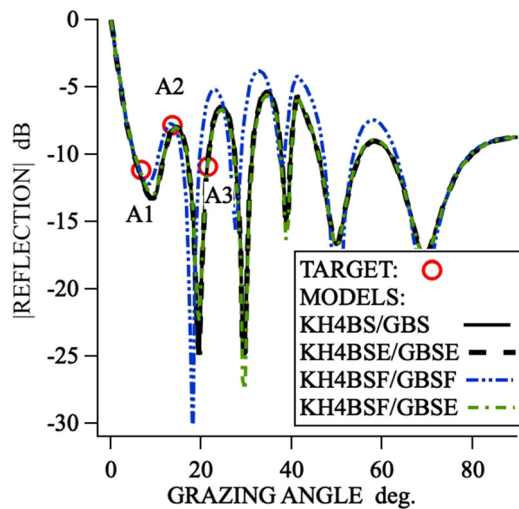
Chotiros et al.

FIG. 11. (Color online) Computed Biot–Stoll plane-wave reflection coefficients of a 4.8 m thick surficial layer over the sediment and the corresponding elastic and fluid approximations (KH4BS, KH4BSE, KH4BSF, GBS, GBSE, and GBSF).

mismatch between model and measurement is even worse at A3, where the measured peak is delayed and wider than the model prediction. It involves one more bottom reflection than A2 and therefore a greater sensitivity to bottom depth variations.

Combinations of the Biot–Stoll model and the elastic and fluid approximations are compared in Fig. 11. For the surficial layer, the same result is obtained whether one chooses the Biot–Stoll model KH4BS or its elastic KH4BSE or fluid KH4BSF approximations. Therefore, the surficial layer may be approximated as fluid layer. In the case of the sediment, the elastic approximation GBDE is indistinguishable from the Biot–Stoll model GBS, but the fluid approximation GBSF gives a different result, indicating that the sediment

needs to have an elastic model. With reference to Fig. 12, it appears that the fluid approximation GBSF may suffice for A1 and A2 but not A3. The fact that there were no significant differences between the GBS and the GBSE suggests that the relative motion between pore fluid and skeletal frame has negligible effect. This is consistent with the very low values of the estimated permeability, $1.65E-15$ and $1.71E-13$ m$^2$ in GBS and KH4BS, respectively. It is not expected that any other reflections can be detected in the measured signal because, beyond A3, the measured signal level bottomed out at the noise floor.

### F. Bottom reflection decay tail

Finally, the remaining energy trailing the bottom reflected signal peaks needs some discussion. There are decay tails that appear to be associated with the bottom signals A1, A2, and A3. It is possible to fit sloping lines to them with a slope of $-10$ dB/s, an exponential decay. At A1 and A2, the decay tail starts at an offset of 6 dB below the peak. The offset for A3 is different. Decay tails are often seen in acoustic signals reflected by the bottom, and they are usually attributed to scattering. There are many possible causes, including bottom roughness, volume inhomogeneities, or even features related to gas hydrates. It is noticed that the seabed under the acoustic path is in the gas hydrate stability zone (GHSZ) as indicated in Fig. 1, which means that the conditions are conducive for the formation of gas hydrates. However, there is not enough information to determine the cause of the scattering at this point, and it could be a subject for future study. If these decay tails can be modeled, then all of the measured bottom-related acoustic energy can be accounted for.

### V. CONCLUSION

The acoustic transmission signals collected in the UNDER-ICE experiment, which took place under ice cover in the Fram Strait, contained a significant proportion of seabed interactions, particularly reflection and scattering. Although the original experiment was not designed to measure the acoustics of the seabed, it contains useful information that may be extracted to characterize the seabed. The latest extended Biot model of acoustic propagation in a porous medium (CREB) was applied. The advantage of this approach is that geophysical parameters, such as mean grain size, porosity, and consolidation coefficient are directly related to acoustic properties, including wave speeds and attenuations. However, for computation efficiency, simpler elastic and fluid approximations were identified and used where possible.

Published seismic, refraction, gravimetric, and core data were used to construct a layered model of the sediment. Profiles of the porosity, p- and s-wave speeds, density, and consolidation coefficient as a function of depth were estimated. Pride's model of sediment consolidation was used to quantify depth dependence, and the shear wave speed profile was found to agree with Hamilton's measurements. Revil's
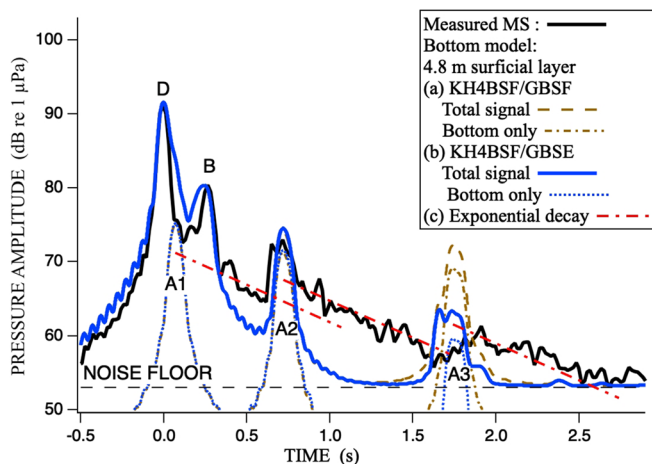


FIG. 12. (Color online) Comparison of the measured signal ensemble average with the propagation model consisting of a surficial layer over a sediment. The surficial layer is approximated as a fluid (KH4BSF). The sediment is approximated either as an elastic solid (GBSE) or a fluid (GBSF). Exponential decay tails at a slope of $-10$ dB/s are compared to the measured signal.

J. Acoust. Soc. Am. **149** (1), January 2021

Chotiros *et al.* 381

relationships were used to estimate the fluid dynamic parameters. The sediment was numerically modeled using a step-wise approximation of the profiles as a layered Biot–Stoll porous medium, using the OASES software suite. The resulting shear wave speed profile suggests that the sediment is over-consolidated, most likely due to the overburden of the ice cover during the last ice age. At the acoustic frequency of interest, i.e., 900 Hz, only the top sediment layer was significant. The elastic approximation, which gave identical results, was used in the numerical computations. The fluid approximation gave significantly different results, indicating that the shear waves could not be ignored.

The measured acoustic signal levels suggest that there is also a thin surficial layer over the sediment, which was not detected by the seismic surveys. This layer was likely deposited after the last ice age and does not show any signs of over-consolidation. The properties of the surficial layer were estimated from mean grain size and porosity. By adjusting the thickness of the surficial layer, it was possible to match the measured acoustic signal levels. The fluid approximation was quite adequate for the surficial layer. The final seabed model consisted of a surficial layer 4.8 m thick, approximated by a fluid, over a sediment half-space approximated as an elastic solid.

There are a few unresolved issues that should be further investigated. One issue is the acoustic propagation channel under the ice, which is not well modeled and is beyond the scope of this study. The other issue is the diffuse or scattered energy trailing the bottom reflected signal peaks. It has the appearance of exponential decay tails and is probably caused by scattering. There are a number of candidate models, such as scattering by seabed roughness or volume scattering due to inclusions, such as drop stones, in the surficial layer, or even gas hydrates, but more research is needed to make a positive determination.

## ACKNOWLEDGMENTS

## APPENDIX A

This appendix gives a summary of the methods used to estimate the Biot–Stoll input parameters, as listed in Table III, from the mean grain size and porosity. The extended Biot (EB) model includes the effects of squirt flow at the grain-grain contact. The Revil relationships were added (REB) to improve estimation of the hydrodynamic parameters. The model was corrected (CREB) to accommodate the sparser skeletal frame of silts and clays. CREB is backward compatible with Biot–Stoll. A brief review of the model and particularly the input parameter estimation is given below.

With reference to Table III, the Biot–Stoll parameters may be divided into three groups: bulk, fluid dynamic, and frame properties. The bulk properties include the density and bulk modulus of the constituent materials, i.e., the solid grains and pore fluid. These are well bounded for seabed sediments. The pore fluid is the seawater at the seabed, which is a function of temperature, depth, and salinity. The most common solid mineral particles are silicates, with a typical density in the region of 2.7 g/cc and a bulk modulus of about 32 GPa. The pore water properties are governed by the depth, salinity, and temperature and are well tabulated. Porosity is the volume of pore water as a fraction of the total bulk volume.

The fluid dynamic properties govern the relative motion between pore fluid and the solid skeletal frame, which is one of the main loss mechanisms. The parameters include viscosity of the pore water, permeability, pore size, and the added mass coefficient, also known as tortuosity, of the skeletal frame. The viscosity of seawater near freezing temperatures is 0.0018 Pa-s (Nayar *et al.*, 2016). The other fluid dynamic properties can be problematic, but they may be estimated using relationships developed by Revil and Cathles (1999) and reiterated by Glover and Walker (2009). The starting point is the Archie relationship between the form factor $F$, porosity $\beta$, and cementation exponent $m$ [Eq. 5.1.2 in Revil and Cathles (1999)] and the added mass coefficient, also known as tortuosity, $c_m$,

$$F = \beta^{-m}; \quad c_m = F\beta = \beta^{1-m}. \tag{A1}$$

It was shown in Glover and Walker (2009) that, if the flow through the pores may be treated as a flow through cylindrical tubes, then the effective pore radius of the tubes, $r_{eff}$, is related to an effective grain diameter, $d_{eff}$, the formation factor $F$, and a parameter $a_B$ by

$$r_{eff}^2 = d_{eff}^2 \frac{2}{a_B m^2 F^2}. \tag{A2}$$

In the context of the Biot theory, the grain diameter $d_{eff}$ may be equated to the mean grain diameter, and the effective pore radius $r_{eff}$ to the pore size $a_p$, giving a direct relationship between porosity, grain size, and pore size. The permeability is related to the effective pore radius by

$$\kappa = \frac{r_{eff}^2}{8F}. \tag{A3}$$

The above equations give direct relationships for the three hydrodynamic parameters in terms of the porosity and grain size and two internal parameters, $m$ and $a_B$. For sands of quasi-spherical grains, they are typically 1.5 and 8/3, respectively. As the grains become smaller, transitioning from sand to silt and then to clay, $m$ changes from 1.5 to 4. Inversion of the value of $a_B$ from a number of data sets yielded values between 1 and 12, with an average value close to 4.

The frame properties quantify the elasticity of the skeletal frame formed by the interconnected grains. The bulk and

shear moduli may be constructed from the grain-grain contact stiffness. The tangential contact stiffness is only dependent on the solid contact, but the normal stiffness is a combination of the solid contact and the dynamics of a liquid film surrounding the solid contact. The starting point is the stiffness of the contact between two grains, idealized as a circular area of contact between two spheres. At the solid contact between two elastic spheres, the normal and tangential contact stiffness, $k_c$ and $g_c$, are given in terms of the contact thickness $h$ and radius $a_s$ and the material bulk and shear moduli $k_r$ and $\mu_r$. In addition, if the contact is mediated by a thin film of liquid, the high-frequency asymptotic normal stiffness $k_y$ would be related to the radius of the film $a_f$ and the bulk modulus of the liquid $k_f$. The bulk and shear moduli of the solid are related by Poisson's ratio, $\nu_r$.

$$k_c = \frac{\pi a_s^2}{h} k_r; \quad k_y = \frac{\pi a_f^2}{h} k_f; \quad g_c = \frac{\pi a_s^2}{h} \mu_r;$$
$$\mu_r = \frac{3(1 - 2\nu_r)}{2(1 + \nu_r)} k_r. \tag{A4}$$

The tangential contact stiffness $S_t$ is a function of the solid contact radius $a_s$ and independent of frequency. The total normal contact stiffness $S_n$ is the sum of the solid contact stiffness and a frequency-dependent component due to the squirt flow associated with the liquid film, characterized by a relaxation frequency $f_k$. For this reason, it is complex and frequency dependent.

$$S_n = k_c + k_y \left( 1 - \frac{2J_1(\kappa_a)}{\kappa_a J_0(\kappa_a)} \right); \quad \kappa_a = \sqrt{-i2\pi \frac{f}{f_k}}. \tag{A5}$$

The contact stiffness may be up-scaled to the frame bulk and shear moduli, $K_b$ and $G$, using the relationships developed by Walton (1987) and reformulated in *The Rock Physics Handbook* (Mavko *et al.*, 1998). In terms of the grain radius $R_g$, the porosity $\beta$, and the average number of contacts at each grain $n$, frame bulk modulus is given by

$$K_b = \frac{n(1 - \beta)}{12\pi R_g} S_n. \tag{A6}$$

This expression may be reformulated in terms of frame parameters $K_{bo}$ and $K_y$,

$$K_b = K_{bo} + K_y \left( 1 - \frac{2J_1(\kappa_a)}{\kappa_a J_0(\kappa_a)} \right). \tag{A7}$$

Using the same terminology, the frame shear modulus is given by

$$G = K_{bo} \frac{9(1 - \nu_r)}{5(2 - \nu_r)} + \frac{3}{5} F_G K_b. \tag{A8}$$

Both $K_b$ and $G$ are complex numbers that are frequency dependent because they are both dependent on $S_n$. The imaginary components represent the second loss mechanism (i.e., the losses due to squirt flow at the grain-grain contacts). These relationships, originally developed for sand, have been "corrected" to accommodate silt and clay with the addition of a porosity-dependent parameter $F_G$ (Chotiros, 2017). This parameter is equal to 1 in sands and coarse silt. For finer silts and clays, its value tends toward zero as porosity increases. It represents the reduction in "jamming" of adjacent grains under shear strain in the sparser skeletal structure of the finer sediments. Rather than parameterizing the grain diameter, contact thickness, and radius, it is more convenient to parameterize the bulk parameters $K_{bo}$, $K_y$, and $f_k$. The statistical connection of these parameters to grain size is shown in Table VI. The connection between $F_G$ and porosity is given in Table VII. The real and imaginary parts of $K_b$ and $G$ are computed at the center of the frequency band, in this case 900 Hz. In the OASES implementation of Biot–Stoll, the imaginary parts of $K_b$ and $G$ are input as attenuations, $a_s$ and $a_c$, with the dimensions of dB per wavelength, and computed as the ratio of the imaginary part to the real part multiplied by $20\pi\log(e)$. The resulting Biot–Stoll parameter values for the surficial layer estimated from the box cores, in the units required for OASES, are shown in Table V, and those for the deeper sediment are shown in Table III.

In summary, the Biot–Stoll parameters may be estimated from measured porosity and grain size as follows. The bulk parameters, $\rho_f$, $\rho_r$, $k_f$, and $k_r$, and the viscosity $\eta$ are tabulated values given in Table III. The fluid dynamic properties $\kappa$, $a_p$, and $c$ are computed from Eqs. (A1)–(A3) using values of $m$ and $a_B$ interpolated from the grain size using Table VI. Finally, the frame bulk and shear moduli are computed using Eqs. (A5)–(A7). The values of $K_y$ and $f_k$ are interpolated from grain size using Table VI, and the value of $F_G$ is interpolated from porosity using Table VII. For the surficial layer, which is unconsolidated, the value of $K_{bo}$ is also interpolated from grain size using Table VI. For the sediment, which is consolidated, the value of $K_{bo}$ is computed from the consolidation parameter using Eq. (6) or inverted from the low-frequency p-wave speed.

## APPENDIX B

The Rayleigh reflection equation as defined on p. 256 of Jackson and Richardson (2006) gives the reflection coefficient $V_{ww}$ in terms of the impedance ratio $z_{wp}$,

TABLE VI. CREB model internal parameters as a function of mean grain size $M_z$.

| $M_z(\phi)$ | −7.0 | −4.0 | −1.5 | −0.5 | 0.5 | 1.5 | 2.5 | 3.5 | 5.0 | 7.0 | 9.0 | 11.0 |
|---|---|---|---|---|---|---|---|---|---|---|---|---|
| $m$ | 1.50 | 1.50 | 1.50 | 1.50 | 1.50 | 1.52 | 1.71 | 2.06 | 2.75 | 3.63 | 4.00 | 4.00 |
| $K_{bo}$ (Pa) | $2.1 \times 10^7$ | $2.1 \times 10^7$ | $2.1 \times 10^7$ | $2.1 \times 10^7$ | $2.1 \times 10^7$ | $2.0 \times 10^7$ | $1.7 \times 10^7$ | $1.3 \times 10^7$ | $5.7 \times 10^6$ | $1.0 \times 10^6$ | $1.0 \times 10^{00}$ | $1.0 \times 10^{-4}$ |
| $K_y$ (Pa) | $2.5 \times 10^8$ | $2.5 \times 10^8$ | $2.5 \times 10^8$ | $2.5 \times 10^8$ | $2.5 \times 10^8$ | $2.5 \times 10^8$ | $2.5 \times 10^8$ | $2.5 \times 10^8$ | $2.5 \times 10^8$ | $2.2 \times 10^8$ | $1.2 \times 10^8$ | $7.3 \times 10^7$ |
| $f_k$ (Hz) | 2000 | 2000 | 2000 | 2000 | 2000 | 90 000 | 2000 | 2000 | 1707 | 292.90 | 0.01 | 0.01 |

TABLE VII. The internal parameter FG as a function of porosity.

| Porosity | 0.2 | 0.3 | 0.4 | 0.5 | 0.6 | 0.7 | 0.8 | 0.9 |
|---|---|---|---|---|---|---|---|---|
| $F_G$ | $9.8 \times 10^{-1}$ | $9.5 \times 10^{-1}$ | $8.1 \times 10^{-1}$ | $4.4 \times 10^{-1}$ | $9.0 \times 10^{-2}$ | $6.9 \times 10^{-3}$ | $1.7 \times 10^{-4}$ | $2.8 \times 10^{-7}$ |

$$V_{ww} = \frac{z_{wp} - 1}{z_{wp} + 1}; \quad z_{wp} = \frac{z_p}{z_w}. \tag{B1}$$

$$z_w = \frac{c_w \rho_w}{\sin(\theta_w)}; \quad z_p = \frac{c_p \rho_p}{\sin(\theta_p)}; \quad \frac{c_w}{\cos(\theta_w)} = \frac{c_p}{\cos(\theta_p)}. \tag{B2}$$

Relationships between mean grain size $M_z$, density ratio $a_\rho$, sound speed ratio $v_p$, and attenuation $k$ (in dB/m/kHz) from pp. 313–314 of Jackson and Richardson (2006) are reproduced below.

$$a_\rho = 0.007797M_z^2 - 0.17057M_z + 2.3139;$$
$$-1 < M_z < 1 \tag{B3}$$

$$a_\rho = -0.0165406M_z^3 + 0.2290201M_z^2$$
$$- 1.1069031M_z + 3.0455; \quad 1 < M_z < 5.3 \tag{B4}$$

$$a_\rho = -0.0012973M_z + 1.1565; \quad 5.3 < M_z < 9 \tag{B5}$$

$$v_p = 0.002709M_z^2 - 0.056452M_z + 1.2778;$$
$$-1 < M_z < 1 \tag{B6}$$

$$v_p = -0.0014881M_z^3 + 0.0213937M_z^2$$
$$- 0.1382798M_z + 1.3425; \quad 1 < M_z < 5.3 \tag{B7}$$

$$v_p = -0.0024324M_z + 1.0091; \quad 5.3 < M_z < 9 \tag{B8}$$

$$k = -0.4566; \quad -1 < M_z < 0 \tag{B9}$$

$$k = 0.1245M_z + 0.1978; \quad 2.6 < M_z < 4.5 \tag{B10}$$

$$k = 0.20098M_z^2 - 2.5228M_z + 8.0399; \quad 4.5 < M_z < 6.0 \tag{B11}$$

$$k = 0.0117M_z^2 - 0.2041M_z + 0.9431; \quad 6.0 < M_z < 9.5 \tag{B12}$$

$$k = 0.0601; \quad 9.5 < M_z \tag{B13}$$

## References

Applied Physics Laboratory, University of Washington (**1994**). "APL-UW high-frequency ocean environmental acoustic models handbook," Technical Report APL-UW 9407.

Bachrach, R., Dvorkin, J., and Nur, A. (**2000**). "Seismic velocities and Poisson's ratio of shallow unconsolidated sands," Geophysics **65**(2), 559–564.

Buckingham, M. J. (**2007**). "On pore-fluid viscosity and the wave properties of saturated granular materials including marine sediments," J. Acoust. Soc. Am. **122**(3), 1486–1501.

Chotiros, N. P. (**2017**). *Acoustics of the Seabed as a Poroelastic Medium* (Springer, Cham, Switzerland).

Colosi, J. A., Scheer, E. K., Flatté, S. M., Cornuelle, B. D., Dzieciuch, M. A., Munk, W. H., Worcester, P. F., Howe, B. M., Mercer, J. A., Spindel, R. C., Metzger, K., Birdsall, T. G., and Baggeroer, A. B. (**1999**). "Comparisons of measured and predicted acoustic fluctuations for a 3250-km propagation experiment in the eastern North Pacific ocean," J. Acoust. Soc. Am. **105**(6), 3202–3218.

Dethleff, D., and Gesa, K. (**2010**). "Fram Strait sea-ice sediment provinces based on silt and clay compositions identify Siberian Kara and Laptev seas as main source regions," Polar Res. **29**, 265–282.

Geissler, W. H., and Jokat, W. (**2004**). "A geophysical study of the northern Svalbard continental margin," Geophys. J. Int. **158**(1), 50–66.

Geissler, W. H., Jokat, W., and Brekke, H. (**2011**). "The Yermak plateau in the Arctic ocean in the light of reflection seismic data-implication for its tectonic and sedimentary evolution," Geophys. J. Int. **187**(3), 1334–1362.

Geissler, W. H., Pulm, P. V., Jokat, W., and Gebhardt, A. C. (**2014**). "Indications for the occurrence of gas hydrates in the Fram Strait from heat flow and multichannel seismic reflection data," J. Geol. Res. **2014**, 1–12.

Glover, P. W. J., and Walker, E. (**2009**). "Grain-size to effective pore-size transformation derived electrokinetic theory," Geophysics **74**(1), E17–E29.

Hamilton, E. L. (**1980**). "Geoacoustic modeling of the sea floor," J. Acoust. Soc. Am. **68**(5), 1313–1340.

Hope, G., Sagen, H., Storheim, E., Hobæk, H., and Freitag, L. (**2017**). "Measured and modeled acoustic propagation underneath the rough arctic sea-ice," J. Acoust. Soc. Am. **142**(3), 1619–1633.

Jackson, D. R., and Richardson, M. D. (**2006**). ONR: The Underwater Acoustics Series in *High-Frequency Seafloor Acoustics* (Springer, New York), p. 334.

Jokat, W., Weigelt, E., Kristoffersen, Y., Rasmussen, T., and Schöne, T. (**1995**). "New geophysical results from the south-western Eurasian Basin (Morris Jesup Rise, Gakkel Ridge, Yermak Plateau) and the Fram Strait," Geophys. J. Int. **123**, 601–610.

Käss, M., Vedenin, A., Hasemann, C., Brandt, A., and Soltwedel, T. (**2019**). "Community structure of macrofauna in the deep Fram Strait: A comparison between two bathymetric gradients in ice-covered and ice-free areas," Deep-Sea Res. Pt. I **152**, 103102.

Mavko, G., Mukerji, T., and Dvorkin, J. (**1998**). *The Rock Physics Handbook* (Cambridge University Press, Cambridge, UK).

Medwin, H. (**1974**). "Sound phase and amplitude fluctuations due to temperature microstructure in the upper ocean," J. Acoust. Soc. Am. **56**(4), 1105–1110.

Nayar, K. G., Sharqawy, M. H., and Lienhard, J. H., V (**2016**). "MIT seawater thermophysical properties library," http://web.mit.edu/seawater/2017_MIT_Seawater_Property_Tables_r2b.pdf (last accessed January 10, 2021).

Pride, S. R. (**2005**). "Relationships between seismic and hydrological properties," in *Hydrogeophysics* (Springer, Amsterdam), pp. 253–290.

Revil, A., and Cathles, L. M. I. (**1999**). "Permeability of shaly sands," Water Resources Res. **35**(3), 651–662.

Riedel, M., Wallmann, K., Berndt, C., Pape, T., Freudenthal, T., Bergenthal, M., Bünz, S., and Bohrmann, G. (**2018**). "*In situ* temperature measurements at the Svalbard continental margin: Implications for gas hydrate dynamics," Geochem. Geophys. Geosyst. **19**(4), 1165–1177.

Schmidt, H. (**2011**). *Oases Version 3.1: User Guide and Reference Manual* (Massachusetts Institute of Technology, Cambridge, MA).

Stein, R. (**2005**). Scientific Cruise Report of the Arctic Expedition ARK-XX/3 of RV Polarstern in 2004: Fram Strait, Yermak Plateau and East Greenland Continental Margin (Alfred-Wegener-Institut für Polar- und Meeresforschung, Bremerhaven, Germany).

Stoll, R. D., and Kan, T. K. (**1981**). "Reflection of acoustic waves at a water-sediment interface," J. Acoust. Soc. Am. **70**(1), 149–156.

Tarng, J. H., Wang, L. K., Yang, C. C., and McDaniel, S. T. (**1988**). "Arrival time and pulse width of acoustic pulses in a turbulent ocean," J. Acoust. Soc. Am. **84**(5), 1802–1807.

Walton, K. (**1987**). "The effective elastic moduli of a random pack of spheres," J. Mech. Phys. Sol. **35**, 213–226.

Wentworth, C. K. (**1922**). "A scale of grade and class terms for clastic sediments," J. Geol. **30**(5), 377–392.

Worcester, P. F., Cornuelle, B. D., Dzieciuch, M. A., Munk, W. H., Howe, B. M., Mercer, J. A., Spindel, R. C., Colosi, J. A., Metzger, K.,

Birdsall, T. G., and Baggeroer, A. B. (**1999**). "A test of basin-scale acoustic thermometry using a large- aperture vertical array at 3250-km range in the eastern North Pacific Ocean," J. Acoust. Soc. Am. **105**(6), 3185–3201.